Material realization of double-Weyl phonons and phononic double-helicoid surface arcs with $P2_13$ space group

Mingmin Zhong,[1,*] Yilin Han,[1,*] Jianhua Wang,[1,*] Ying Liu,[2,†] Xiaotian Wang,[1,3,‡] and Gang Zhang[4,§]

[1]*School of Physical Science and Technology, Southwest University, Chongqing 400715, China*

[2]*School of Materials Science and Engineering, Hebei University of Technology, Tianjin 300130, China*

[3]*Institute for Superconducting and Electronic Materials (ISEM), University of Wollongong, Wollongong 2500, Australia*

[4]*Institute of High Performance Computing, Agency for Science, Technology and Research (A*STAR), 138632, Singapore*

(Received 10 January 2022; revised 4 July 2022; accepted 25 July 2022; published 4 August 2022)

Unconventional chiral quasiparticles with twofold, threefold, and fourfold degeneracies and Chern number (C) $= \pm 2$ have recently sparked interest because of their topological chirality in momentum space. Herein, based on first-principles calculations and symmetry analysis, we propose 14 synthesized topological phonon systems with space group $P2_13$ (No. 198) that host two types of almost-ideal double-Weyl points, which are the fourfold degenerate charge-2 Dirac point and the threefold degenerate spin-1 Weyl point. Based on the projected local density of states on the [100] and [101] surfaces of these selected realistic materials, we discovered two visible winding around the projected double-Weyl points, demonstrating the appearance of phononic double-helical surface arcs. Furthermore, we constructed a $\boldsymbol{k} \cdot \boldsymbol{p}$ model to determine how the two types of double-Weyl point phonons coexist in the system with the $P2_13$ space group. We believe that this work provides directions for investigating double-Weyl point phonons and an ideal platform for investigating phononic double-helical surface states in realistic materials.

DOI: 10.1103/PhysRevMaterials.6.084201

I. INTRODUCTION

Quantum materials with Weyl points (WPs) [1–3] have sparked a new wave of research in condensed-matter physics. In 2015, Weyl fermions [4,5] were detected as collective electronic excitations in the strong spin-orbit coupled and inversion symmetry breaking crystal tantalum arsenide (TaAs) [6–12]. WPs are typically divided into two categories: conventional WPs [13–16] and unconventional WPs [17–21]. The conventional WPs are contributed by two degenerate bands with a monopole charge of ± 1. Conventional Weyl fermions occur in three-dimensional (3D) crystals that lack inversion symmetry or time-inversion symmetry or both. Unconventional WPs with a Chern number (C) larger than one are enabled by additional crystal symmetry.

We point out that a topological charge can result in many intriguing electronic, optical, and magnetic phenomena, all of which are strongly influenced by the sign of the topological charge, e.g., the chirality. The topological chirality in momentum space may result in many physical properties [22–26], including unique spin texture, large helicoid Fermi arcs, large topologically nontrivial energy windows, quantized circular photogalvanic effects, chiral magnetic effects, and unconventional superconductivity.

The double-WP, which is of twofold degeneracy, is a prominent example of an unconventional WP. Thus far, double-WPs with topological charges have been widely studied in electronic systems [27,28]. Contrary to conventional WPs, double-WPs have a linear dispersion along one direction and a quadratic energy splitting in the plane normal to the direction [see Fig. 1 (a)]. In Ref. [29], Fang *et al.* discussed that the fourfold and sixfold rotation symmetries are responsible for the presence of double-WPs. Moreover, the double-WPs have been demonstrated to have a C of ± 2. Generally, the following effective model can be used to describe it:

$$\mathcal{H}_{C-2\ WP} = c_1 k_z + c_2 k_\parallel^2 + c_3 k_z \sigma_3 + (\alpha k_+^2 \sigma_+ + \text{H.c.}), \quad (1)$$

where $k_\parallel = \sqrt{k_x^2 + k_y^2}$, $k_+ = k_x + i k_y$, and $\sigma_+ = (\sigma_x + i\sigma_y)/2$. Furthermore, as shown in Figs. 1(b) and 1(c), there are two additional unconventional WPs with threefold and fourfold degeneracies and a topological charge of ± 2, respectively. Remarkably, the second type double-WP is expected to resemble a spin-1 (S-1) quasiparticle model, denoted as S-1 WP. The third type is of fourfold degeneracy, denoted as C-2 Dirac point (DP). It contains two C-1 WPs with the same topological charge.

Very recently, the studies on double-WPs have been extended to spinless phonon systems [30–32]. Phonons are bosons that are unaffected by the spin-orbit coupling effect and not limited by the Fermi level. Additionally, the discovery of topological phonons [33–42] provides us with a potential platform to investigate heat transfer, phonon scattering, and electron-phonon interaction. For example, Zhang *et al.* [31] proposed a series of noncentrosymmetric materials, MSi (M = Fe, Co, Mn, Re, and Ru), hosting double-WPs in their phonon dispersions by employing first-principles calculations. Miao *et al.* [43] were motivated by Ref. [31] and used inelastic x-ray scattering to measure the phonon dispersion in FeSi,

*These authors contributed equally to this work.
†Corresponding author: ying_liu@hebut.edu.cn
‡Corresponding author: xiaotianwang@swu.edu.cn
§Corresponding author: zhangg@ihpc.a-star.edu.sg

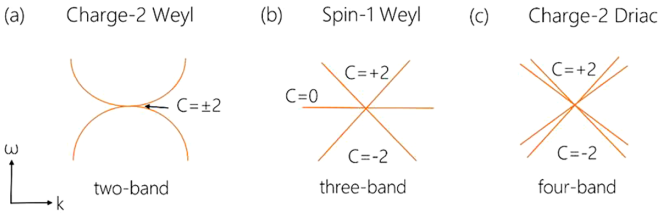

FIG. 1. Various types of double-WPs: (a) C-2 WP, (b) S-1 WP, and (c) C-2 DP.

resulting in the first observation of double-Weyl phonons in an experiment. Furthermore, the work of Jin *et al.* [44] establishes a link between different types of double-Weyl phonons and provides directions for investigating transitions between these unconventional quasiparticles.

As a good candidate with double-Weyl phonons, the material should at least satisfy the following requirements. First, it is crucial that no other extraneous phonon bands are nearby in a certain frequency, since otherwise they may complicate the interpretation of measured properties. Second, the topological surface modes, arising from the projections of the crossing points, should greatly facilitate the experimental detection. That is, the arc-shaped surface modes of candidate materials with double-Weyl phonons should be as visible as possible (i.e., not covered by the bulk phonon modes). Third, the material should be stable and easy to synthesize. These conditions limit the suitable candidate materials, and currently, there is still an urgent need to search for realistic material systems to realize the double-Weyl phonons.

In this work, using the first-principles calculations and symmetry analysis, we show that 14 realistic materials with the $P2_13$ space group have two different types of ideal double-Weyl phonons (i.e., S-1 WP and C-2 DP phonons) in their phonon band structures. Meanwhile, these double-Weyl phonons can induce double-helicoid surface arcs, which are two visible arcs that wind around the projected double-WPs (at $\overline{\mathrm{R}}$ and $\overline{\Gamma}$ points). Furthermore, a detailed $\boldsymbol{k}\cdot\boldsymbol{p}$ model was constructed to analyze the physics of the two types of double-Weyl phonons that coexist in these phonon systems. These reported realistic materials, which have a $P2_13$-type structure, are expected to be promising ideal targets for realizing double-Weyl phonons and double-helicoid surface states in experiments.

II. COMPUTATIONAL METHODS AND MATERIAL CANDIDATES

The ground state of the materials was determined using the density-functional theory [45], and the exchange-correlation functional was handled using the generalized gradient approximation [46] with the Perdew-Burke-Ernzerhof [47] functional. Additionally, the projector augmented-wave method [48] was used for interactions between ions and valence electrons, and a cutoff energy of 500 eV was set during the calculations. We used a Γ-centered k mesh of 9×9×9 for Brillouin zone (BZ) sampling. Furthermore, dynamic lattice calculations were performed to obtain the phonon dispersions of the materials using the density-functional perturbation theory, as implemented in the PHONOPY package [49]. The topological signatures of the [100] and [101] phonon surface states were calculated by constructing a Wannier tight-binding Hamiltonian of phonons [50]. The Wilson loop approach [51,52] was used to calculate the Chern number C on a sphere enclosing the Weyl node by tracking the evolution of the hybrid Wannier charge centers. In this work, we selected 14 realistic material candidates with the $P2_13$ space group. These 14 materials are HfSO, SnRh, GeRh, AsPdS, CaPtSi, NiSbS, SrPIr, SrSiPd, SbIrS, BiIrS, BaPIr, NiAsS, AlPt, and AlPd materials. They are all realistic materials [53–64]. To determine the magnetic ground state of above materials, an energy comparison was made among three different configurations: ferromagnetic, antiferromagnetic, and the nonmagnetic systems, with the help of density functional theory calculations. The magnetic ground state for these materials is nonmagnetic state (see Fig. S1 in Supplemental Material (SM) [65]). We optimized the lattice constants for these 14 materials, and the obtained lattice constants alongside the previous experimental lattice constants are shown in Table I.

TABLE I. Experimental and theoretical lattice constants of HfSO, SnRh, GeRh, AsPdS, CaPtSi, NiSbS, SrPIr, SrSiPd, SbIrS, BiIrS, BaPIr, NiAsS, AlPt, and AlPd.

Materials	Experimental lattice constants (a/b/c)	Theoretical lattice constants (a/b/c)
HfSO	5.682 Å [53]	5.738 Å
SnRh	5.122 Å [54]	5.213 Å
GeRh	4.862 Å [55]	4.951 Å
AsPdS	5.949 Å [56]	6.033 Å
CaPtSi	6.320 Å [57]	6.384 Å
NiSbS	5.881 Å [58]	5.960 Å
SrPIr	6.325 Å [59]	6.384 Å
SrSiPd	6.500 Å [60]	6.569 Å
SbIrS	6.025 Å [61]	6.104 Å
BiIrS	6.143 Å [56]	6.224 Å
BaPIr	6.531 Å [62]	6.551 Å
NiAsS	5.688 Å [58]	5.710 Å
AlPt	4.865 Å [63]	4.918 Å
AlPd	4.859 Å [64]	4.909 Å

We used only the ternary cubic HfSO system [53] as a typical example to demonstrate its double-Weyl phonon behavior in the following discussion because all 14 materials belong to the same space group, i.e., $P2_13$-type. Figure 2(a) depicts the crystal structure of $P2_13$-type HfSO, which

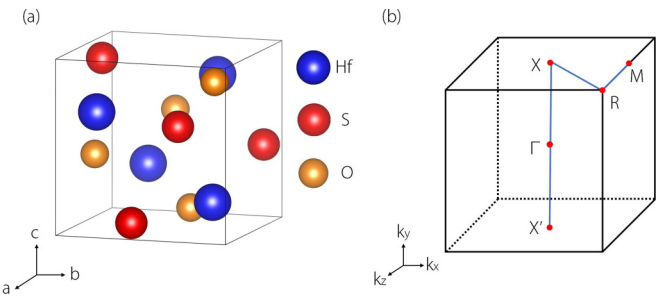

FIG. 2. (a) Crystal structure of $P2_13$-type HfSO and (b) bulk BZ and selected symmetry paths (blue lines).

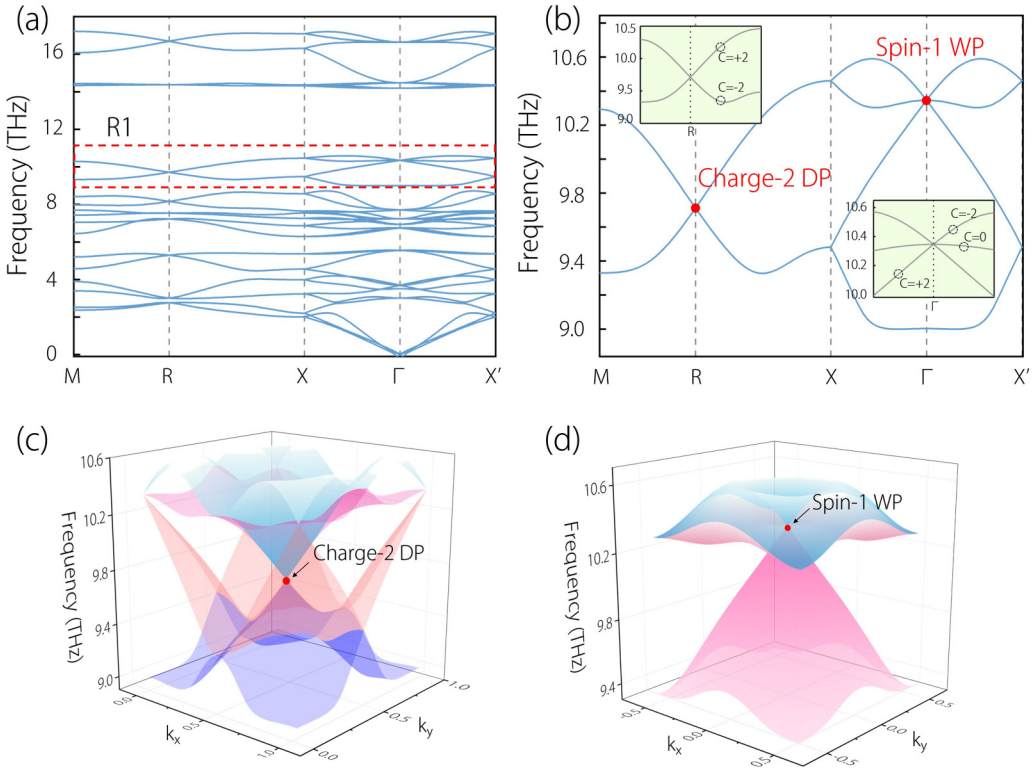

FIG. 3. (a) Phonon dispersion of HfSO along the M-R-X-Γ-X' paths. (b) The enlarged phonon dispersion in the R1 region. The inset figures (green boxes) show the C of the bands around the C-2 DP and S-1 WP. The three bands around the S-1 WP are labeled $C = +2, -2$, and 0, respectively. The four bands around the C-2 DP are labeled as $C = +2$, and –2, respectively. Three-dimensional phonon bands around the (c) C-2 DP and (d) S-1 WP.

contains 12 atoms in its unit cell, with four Hf atoms occupying the 4a (0.681476, 0.818523, 0.181476) and 4a (0.318523, 0.318523, 0.318523) Wyckoff positions, four S atoms at the 4a (0.919353, 0.419353, 0.080646) and 4a (0.580646, 0.580646, 0.580646) Wyckoff positions, and four O atoms situated at the 4a (0.403952, 0.596047, 0.096047) and 4a (0.903952, 0.903952, 0.903952) Wyckoff positions. Based on the first-principles calculations, the crystal structure of HfSO is completely relaxed, and the equilibrium lattice constants are a = b = c = 5.738 Å (see Table I), which agrees well with the experimental values (a = b = c = 5.68 Å) [53].

III. ALMOST IDEAL DOUBLE-WEYL PHONONS IN HFSO

Based on the selected M-R-X-Γ-X' symmetry paths in the three-dimensional BZ [Fig. 2(b)], the phonon dispersion of HfSO along the symmetry paths is shown in Fig. 3(a). According to the figure, the HfSO system is dynamically stable because there is no imaginary frequency mode in its phonon dispersion. We mainly focus on the phonon bands in the 9.0- to 10.6-THz frequency region (labeled as R1), which are well separated from the phonon bands in other frequency regions. To further investigate the topology of the phonons in R1, we plotted an enlarged phonon dispersion of this region in Fig. 3(b).

Two evident topological signatures can be observed in R1: the C-2 DP, which has a fourfold degeneracy at the R point, and the S-1 WP, which has a threefold degeneracy at the Γ point. The green boxes in the inset of Fig. 3(b) show the C values of some nontrivial phonon branches around the R and Γ points. The four bands around the R point have a nonzero C of ±2, exhibiting nontrivial topological behavior. Similarly, the three bands around the Γ point have a C of ±2 and 0, respectively, confirming the existence of nontrivial topological S-1 WP at point Γ. The three-dimensional phonon bands around the C-2 DP and S-1 WP are plotted in Figs. 3(c) and 3(d), respectively. The red dots in Figs. 3(c) and 3(d) indicate the C-2 DP and S-1 WP, respectively. Moreover, the C-2 DP and the S-1 WP, at the R and Γ points in R1, can be viewed as almost ideal double-Weyl points due to they are with ultraclean phonon band dispersions.

It is worth noting that the C-2 DP and the S-1 WP in a $P2_13$-type structure are symmetry enforced [66]. We present a detailed symmetry analysis of the C-2 DP and S-1 WP to better understand their physics. The small point group at the Γ point is also the T point group. Importantly, T is the smallest point group that can enforce a S-1 Weyl nodal point [67]. Hence, it could intrinsically protect a threefold band crossing since it has a three-dimensional irreducible representation (IRR). On this basis, the symmetry operations and

time-reversal symmetry (TRS) can be written as

$$C_{3,111} = \begin{pmatrix} 0 & 0 & 1 \\ 1 & 0 & 0 \\ 0 & 1 & 0 \end{pmatrix}, \tag{2}$$

$$C_{2z} = \begin{pmatrix} -1 & 0 & 0 \\ 0 & -1 & 0 \\ 0 & 0 & 1 \end{pmatrix}, \tag{3}$$

$$C_{2y} = \begin{pmatrix} -1 & 0 & 0 \\ 0 & 1 & 0 \\ 0 & 0 & -1 \end{pmatrix}, \quad \mathcal{T} = I_{3\times 3}\mathcal{K}. \tag{4}$$

Thereafter, the effective model adopts the form of a S-1 fermion:

$$\mathcal{H}_{\text{S}-1\text{ WP}} = -\gamma \boldsymbol{k} \cdot \boldsymbol{S}, \tag{5}$$

where $\boldsymbol{S}$ is the S-1 matrix, which satisfies the angular momentum algebra $[S_i, S_j] = i\epsilon_{ijk}S_k$. For S-1 WP, the three bands had a C of +2, 0, and –2, respectively [see Fig. 1(b)]. The S-1 WP also had a C-2 topological charge, similarly to the S-1 fermion.

The C-2 DP is located at the R point, which has a small point group belonging to the T point group generated by a threefold rotation along the [111] direction and a double twofold rotation symmetry along the x and y directions, namely $C_{3,111}$, C_{2x}, and C_{2y}. In particular, there are two two-dimensional IRRs in SG 198 that can be connected to each other by the TRS to form a 4D IRR, resulting in a fourfold band crossing. To be specific, the spatial operations and TRS under this 4D IRR take the following forms:

$$C_{3,111} = \frac{\sqrt{2}}{2}\begin{pmatrix} e^{i\frac{5\pi}{12}} & -e^{i\frac{5\pi}{12}} & 0 & 0 \\ -e^{i\frac{\pi}{12}} & -e^{i\frac{\pi}{12}} & 0 & 0 \\ 0 & 0 & e^{-i\frac{5\pi}{12}} & ie^{i\frac{\pi}{12}} \\ 0 & 0 & -e^{-i\frac{\pi}{12}} & -e^{-i\frac{\pi}{12}} \end{pmatrix}, \tag{6}$$

$$C_{2x} = -i\Gamma_{3,1}, \quad C_{2y} = i\Gamma_{02}, \quad \mathcal{T} = i\Gamma_{1,0}\mathcal{K}, \tag{7}$$

where $\mathcal{K}$ is the complex conjugation, $\Gamma_{i,j} = \sigma_i \otimes \sigma_j$ (with $i, j = 1,2,3$), and σ's is the Pauli matrix.

Under the constraints from the symmetries, the effective model satisfies

$$\mathcal{O}(R)H(\boldsymbol{k})\mathcal{O}^{-1}(R) = H(R\boldsymbol{k}), \tag{8}$$

where $\mathcal{O}$ is the matrix representation of the corresponding symmetry operation (R), and R runs across all generating elements. Therefore, the effective model for C-2 DP can be derived as follows:

$$\mathcal{H}_{\text{C}-2\text{ DP}} = c_1 + \begin{bmatrix} -c_2k_z & c_2k_+ & 0 & 0 \\ c_2k_- & c_2k_z & 0 & 0 \\ 0 & 0 & -c_2k_z & -c_2k_- \\ 0 & 0 & -c_2k_+ & c_2k_z \end{bmatrix}, \tag{9}$$

indicating a isotropic C-2 Dirac point. Here c's are real parameters. According to Eq. (9), the C-2 DP is a composition of two isotropic WPs with the same charge, which then contributes to a DP with a doubling charge. In addition, the essential symmetry operations that protect the C-2 Dirac point are the two twofold rotation symmetry. Together with $\mathcal{T}$, they satisfy $(C_{2y}\mathcal{T})^2 = -1$, $\{C_{2x}, C_{2y}\}$ at R point, leading to a C-2 Dirac point, but with an isotropic dispersion in all directions.

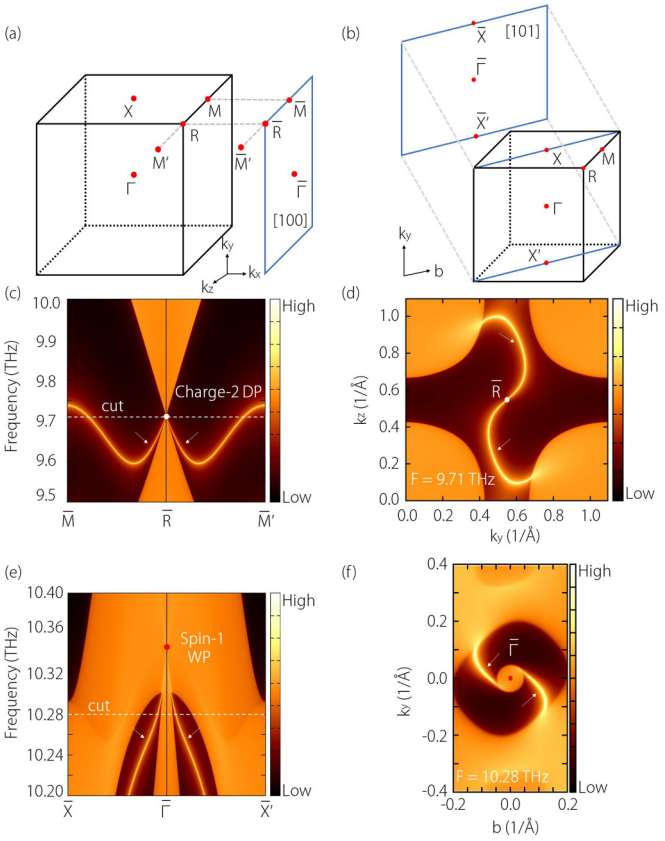

FIG. 4. [(a) and (b)] Bulk BZ and the [100] and [101] surface BZs. (c) The surface local density of states (LDOS) of the phonons on the [100] surface and (d) the isofrequency arcs cut at 9.71 THz. (e) The surface LDOS of the phonons on the [101] surface and (f) the isofrequency arcs cut at 10.28 THz. The nontrivial surface states are indicated by the white arrows in (c)–(f).

IV. PHONONIC DOUBLE-HELICOID SURFACE ARCS IN HFSO

Subsequently, we examined the phononic surface states to further confirm the topological signatures of the C-2 DP and S-1 WP. Figure 4(c) shows the surface local density of states (LDOS) of the phonons on the [100] surface along the $\overline{\text{M}}$-$\overline{\text{R}}$-$\overline{\text{M}}'$ paths [Fig. 4(a)]. The R and M points are projected to $\overline{\text{R}}$ and $\overline{\text{M}}$ in the [100] surface BZ. Figure 4(d) depicts the isofrequency surface contours at 9.71 THz [see the white dotted line in Fig. 4(c)]. As expected, double arc-shaped surface states emerge from the projection of the C-2 DP (i.e., $\overline{\text{R}}$ point), corresponding to the obtained topological charge of the C-2 DP (i.e., $|C| = 2$). In Fig. 4(b), we selected the X′, Γ, and X points in the three-dimensional BZ and projected them to the $\overline{\text{X}}'$, $\overline{\Gamma}$, and $\overline{\text{X}}$ points in the [101] surface BZ. Figures 4(e) and 4(f) show the surface LDOS of the phonons on the [101] surface along the $\overline{\text{X}}$-$\overline{\Gamma}$-$\overline{\text{X}}'$ paths and the isofrequency surface contours at 10.28 THz, respectively. From these figures, the projection of the S-1 WP, i.e., point $\overline{\Gamma}$, can be concluded to produce two arcs that reflect the double arc-shaped surface states. More importantly, the surface states are not covered by the bulk band projection, which could be very beneficial for the experimental detection.

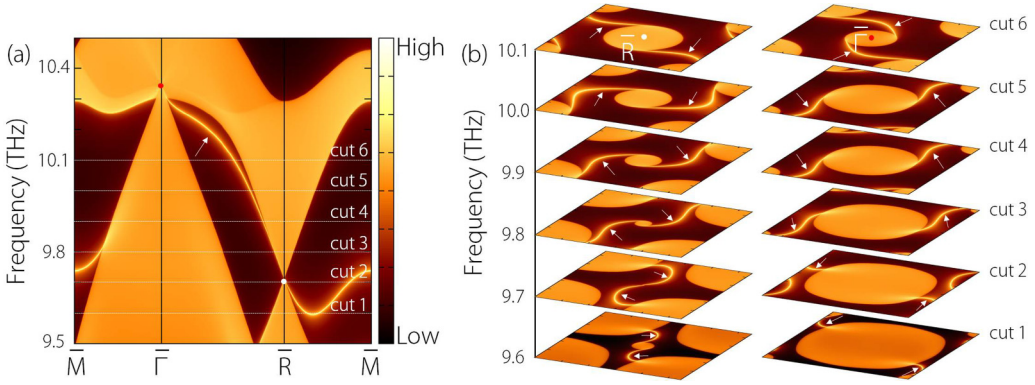

FIG. 5. (a) The surface LDOS of the phonons on the [100] surface and (b) the isofrequency arcs at six frequency cuts (named cuts 1–6). The white arrows in (a) and (b) indicate the double surface arcs connected at the $\overline{\Gamma}$ and $\overline{\mathrm{R}}$ points

In Fig. 4, two surface arcs are observed to be connected to the projected double-Weyl phonons because the $|C|$ of the double-WPs is equal to 2. The two surface arcs are confirmed to be double-helicoid surface arcs. Figure 5(a) depicts the surface LDOS of the phonons along $\overline{\mathrm{M}}$-$\overline{\Gamma}$-$\overline{\mathrm{R}}$-$\overline{\mathrm{M}}$ on the [100] surface. Six frequency cuts (named cuts 1–6) were chosen to exhibit different isofrequency surface contours. Figure 5(b) depicts the results of the different isofrequency surface contours. In this figure, the two double-WPs at Γ and R are projected to $\overline{\Gamma}$ and $\overline{\mathrm{R}}$ in the [100] surface BZ. As the frequency increases from cut 1 to cut 6, two noticeable phononic surface sheets (see white arrows) wind around the projected double-WPs at $\overline{\Gamma}$ and $\overline{\mathrm{R}}$. Two surface arcs wind anticlockwise around the $\overline{\Gamma}$ point, while two surface arcs wind clockwise around the $\overline{\mathrm{R}}$ point. Thus, the projection of the double-WPs would be a double-helicoid [19].

V. ADDITIONAL NOTES

In addition to HfSO, the other 13 material samples with space group $P2_13$ (No. 198) are included in Figs. S2–S14 (see SM [65]), where the almost ideal C-2 DP and S-1 WP can also be observed, to support the inspirational findings of the double-WP phonons. Furthermore, two visible phononic surface arcs are connected to the projected S-1 WP and C-2 DP because of the topological charge of these double-WPs.

The following points are worth noting for the benefit of experimenters: Inelastic x-ray scattering can be used to probe the bulk phonon dispersion in the whole THz frequencies, and thus this technique is recommended for determining the proposed double-Weyl phonons in the material samples used in this study. Some experimental techniques, such as high-resolution electron energy loss spectroscopy, helium scattering, and terahertz spectroscopy, are recommended for detecting the proposed phonon surface states of these material samples.

For the HfSO, we examined the phonon mode displacements of three overlapping bands (No. 26-28) at the Γ point to understand the S-1 WP around 10.30 THz. Moreover, we also calculated the phonon mode displacement of four overlapping bands (No. 25-28) at the R point around 9.80 THz to examine the C-2 DP. The results of the corresponding modes are presented in Fig. S15 (see SM [65]). From Fig. S15, large displacements are observed to arise from the vibration of the O and S elements.

VI. CONCLUSION

In summary, based on first-principles calculations and symmetry analysis, we propose fourteen synthesized $P2_13$-type materials that host two types of almost ideal double-WP (C-2 DP and S-1 WP) phonons. We also calculated the projected LDOS of the selected fourteen materials on the surface BZ. The results show that the visible phononic surface arc around the projection of a double-WP is a double-helicoid arc, meaning that two screw surfaces wind around the projected double-WP. Our theoretical results predict a series of almost ideal realistic materials with double-Weyl phonons. They also determine the occurrence of rare phononic double-helicoid surface arcs and add to the understanding of topological phonons with topological charges.

ACKNOWLEDGMENTS

Y.L. is grateful for the support from the Nature Science Foundation of Hebei Province (No. A2021202002) and HZWTECH for providing computation facilities.

[1] Y. Xu, F. Zhang, and C. Zhang, Phys. Rev. Lett. **115**, 265304 (2015).
[2] A. A. Burkov and L. Balents, Phys. Rev. Lett. **107**, 127205 (2011).
[3] A. A. Soluyanov, D. Gresch, Z. J. Wang, Q. S. Wu, M. Troyer, X. Dai, and B. A. Bernevig, Nature (Lond.) **527**, 495 (2015).
[4] S. Y. Xu, I. Belopolski, N. Alidoust, M. Neupane, G. Bian, C. L. Zhang, R. Sankar, G. Q. Chang, Z. J. Yuan, C. C. Lee, S. M.

Huang, H. Zheng, J. Ma, D. S. Sanchez, B. K. Wang, A. Bansil, F. C. Chou, P. P. Shibayev, H. Lin, S. Jia *et al.*, Science **349**, 613 (2015).

[5] B. Q. Lv, H. M. Weng, B. B. Fu, X. P. Wang, H. Miao, J. Ma, P. Richard, X. C. Huang, L. X. Zhao, G. F. Chen, Z. Fang, X. Dai, T. Qian, and H. Ding, Phys. Rev. X **5**, 031013 (2015).

[6] Y. Xu, S. T. Wang, and L. M. Duan, Phys. Rev. Lett. **118**, 045701 (2017).

[7] P. Li, Y. Wen, X. He, Q. Zhang, C. Xia, Z. M. Yu, S. Y. A. Yang, Z. Y. Zhu, H. N. Alshareef, and X. X. Zhang, Nat. Commun. **8**, 2150 (2017).

[8] P. Li, W. K. Wu, C. H. Zhang, J. W. Zhang, S. F. Zhang, Z. M. Yu, S. Y. A. Yang, A. Manchon, and X. X. Zhang, Nat. Commun. **9**, 3990 (2018).

[9] W. C. Li, L. X. Zhao, H. J. Zhao, G. F. Chen, and Z. X. Shi, Chinese Phys. B **31**, 057103 (2022).

[10] B. Zhao, B. Karpiak, D. Khokhriakov, A. Johansson, A. M. Hoque, X. G. Xu, Y. Jiang, I. Mertig, and S. P. Dash, Adv. Mater. **32**, 2000818 (2020).

[11] Y. A. Liu, Q. Q. Gu, Y. Peng, S. M. Qi, N. Zhang, Y. N. Zhang, X. M. Ma, R. Zhu, L. M. Tong, J. Feng, Z. Liu, and J. H. Chen, Adv. Mater. **30**, 1706402 (2018).

[12] P. Yu, W. Fu, Q. S. Zeng, J. H. Lin, C. Yan, Z. C. Lai, B. J. Tang, K. Suenaga, H. Zhang, and Z. Liu, Adv. Mater. **29**, 1701909 (2017).

[13] X. Wan, A. M. Turner, A. Vishwanath, and S. Y. Savrasov, Phys. Rev. B **83**, 205101 (2011).

[14] N. P. Armitage, E. J. Mele, and A. Vishwanath, Rev. Mod. Phys. **90**, 015001 (2018).

[15] I. Belopolski, D. S. Sanchez, Y. Ishida, P. C. Pan, P. Yu, S. Y. Xu, G. Q. Chang, T. R. Chang, H. Zheng, N. Alidoust, G. Bian, M. Neupane, S. M. Huang, C. C. Lee, Y. Song, H. J. Bu, G. H. Wang, S. S. Li, G. Eda, H. T. Jeng *et al.* Nat. Commun. **7**, 13643 (2016).

[16] Z. M. Yu, Y. Yao, and S. Y. A. Yang, Phys. Rev. Lett. **117**, 077202 (2016).

[17] Y. H. Yang, Z. Gao, X. L. Feng, Y. X. Huang, P. H. Zhou, S. Y. A. Yang, Y. D. Chong, and B. L. Zhang, Phys. Rev. Lett. **125**, 143001 (2020).

[18] B. Bradlyn, J. Cano, Z. J. Wang, M. G. Vergniory, C. Felser, R. J. Cava, and B. A. Bernevig, Science **353**, aaf5037 (2016).

[19] H. L. He, C. Y. Qiu, X. X. Cai, M. Xiao, M. Z. Ke, F. Zhang, and Z. Y. Liu, Nat. Commun. **11**, 1820 (2020).

[20] H.-X. Wang, Z.-K. Lin, B. Jiang, G.-Y. Guo, and J.-H. Jiang, Phys. Rev. Lett. **125**, 146401 (2020).

[21] K. G. Rana, F. K. Dejene, N. Kumar, C. R. Rajamathi, K. Sklarek, C. Felser, and S. S. P. Parkin, Nano Lett. **18**, 6591 (2018).

[22] M. Z. Hasan, G. Q. Chang, I. Belopolski, G. Bian, S. Y. Xu, and J. X. Yin, Nat. Rev. Mater. **6**, 784 (2021).

[23] D. Rees, K. Manna, B. Z. Lu, T. Morimoto, H. Borrmann, C. Felser, J. E. Moore, D. H. Torchinsky, and J. Orenstein, Sci. Adv. **6**, eaba0509 (2020).

[24] Z. C. Rao, H. Li, T. T. Zhang, S. J. Tian, C. H. Li, B. B. Fu, C. Y. Tang, L. Wang, Z. L. Li, W. H. Fan, J. J. Li, Y. B. Huang, Z. H. Liu, Y. W. Long, C. Fang, H. M. Weng, Y. G. Shi, H. C. Lei, Y. J. Sun. T. Qian, and H. Ding, Nature (Lond.) **567**, 496 (2019).

[25] H. Wang, H. C. Wang, Y. Q. Chen, J. W. Luo, Z. J. Yuan, J. Liu, Y. Wang, S. Jia, X. J. Liu, J. Wei, and J. Wang, Sci. Bull. **62**, 425 (2017).

[26] A. Cortijo, D. Kharzeev, K. Landsteiner, and M. A. H. Vozmediano, Phys. Rev. B **94**, 241405(R) (2016).

[27] L. Jin, X. M. Zhang, Y. Liu, X. F. Dai, L. Y. Wang, and G. D. Liu, Phys. Rev. B **102**, 195104 (2020).

[28] W. K. Wu, Z. M. Yu, X. T. Zhou, Y. X. Zhao, and S. Y. A. Yang, Phys. Rev. B **101**, 205134 (2020).

[29] C. Fang, M. J. Gilbert, X. Dai, and B. A. Bernevig, Phys. Rev. Lett. **108**, 266802 (2012).

[30] R. Wang, B. W. Xia, Z. J. Chen, B. B. Zheng, Y. J. Zhao, and H. Xu, Phys. Rev. Lett. **124**, 105303 (2020).

[31] T. Zhang, S. Song, A. Alexandradinata, H. Wen, C. Fang, L. Lu, and Z. Fang, Phys. Rev. Lett. **120**, 016401 (2018).

[32] G. Ding, F. Zhou, Z. Zhang, Z.-M. Yu, and X. Wang, Phys. Rev. B **105**, 134303 (2022).

[33] Q. B. Liu, Z. J. Wang, and H. H. Fu, Phys. Rev. B **103**, L161303 (2021).

[34] Q. B. Liu, Y. T. Qian, H. H. Fu, and Z. J. Wang, npj Comput. Mater. **6**, 95 (2020).

[35] Q. B. Liu, Z. Q. Wang, and H. H. Fu, Phys. Rev. B **104**, L041405 (2021).

[36] Y. Z. Liu, X. B. Chen, and Y. Xu, Adv. Funct. Mater. **30**, 1904784 (2020).

[37] Y. Z. Liu, C. S. Lian, Y. Li, Y. Xu, and W. H. Duan, Phys. Rev. Lett. **119**, 255901 (2017).

[38] Y. Liu, N. Zou, L. Zhao, X. Chen, Y. Xu, and W. Duan, Nano Lett. **22**, 2120 (2022).

[39] B. W. Xia, R. Wang, Z. J. Chen, Y. J. Zhao, and H. Xu, Phys. Rev. Lett. **123**, 065501 (2019).

[40] Z. J. Chen, R. Wang, B. W. Xia, B. B. Zheng, Y. J. Jin, Y. J. Zhao, and H. Xu, Phys. Rev. Lett. **126**, 185301 (2021).

[41] J. Li, L. Wang, J. Liu, R. Li, Z. Zhang, and X. Q. Chen, Phys. Rev. B **101**, 081403(R) (2020).

[42] J. X. Li, J. X. Liu, S. A. Baronett, M. F. Liu, L. Wang, R. H. Li, Y. Chen, D. Z. Li, Q. Zhu, and X. Q. Chen, Nat. Commun. **12**, 1204 (2021).

[43] H. Miao, T. T. Zhang, L. Wang, D. Meyers, A. H. Said, Y. L. Wang, Y. G. Shi, H. M. Weng, Z. Fang, and M. P. M. Dean, Phys. Rev. Lett. **121**, 035302 (2018).

[44] Y. J. Jin, Z. J. Chen, X. L. Xiao, and H. Xu, Phys. Rev. B **103**, 104101 (2021).

[45] R. G. Parr, Annu. Rev. Phys. Chem. **34**, 631 (1983).

[46] J. P. Perdew, K. Burke, and M. Ernzerhof, Phys. Rev. Lett. **77**, 3865 (1996).

[47] J. P. Perdew, K. Burke, and M. Ernzerhof, Phys. Rev. Lett. **80**, 891 (1998).

[48] P. E. Blöchl, Phys. Rev. B **50**, 17953 (1994).

[49] A. Togo and I. Tanaka, Scr. Mater. **108**, 1 (2015).

[50] Q. S. Wu, S. N. Zhang, H. F. Song, M. Troyer, and A. A. Soluyanov, Comput. Phys. Commun. **224**, 405 (2018).

[51] R. Yu, X. L. Qi, A. Bernevig, Z. Fang, and X. Dai, Phys. Rev. B **84**, 075119 (2011).

[52] D. Gresch, G. Autes, O. V. Yazyev, M. Troyer, D. Vanderbilt, B. A. Bernevig, and A. A. Soluyanov, Phys. Rev. B **95**, 075146 (2017).

[53] K. Stocks, G. Eulenberger, and H. Hahn, Z. Anorg. Allg. Chem. **463**, 105 (1980).

[54] K. Schubert, Z. Naturforsch. A **2**, 120 (1947).
[55] V. I. Larchev and S. V. Popova, J. Less Common Met. **87**, 53 (1982).
[56] F. Hulliger, Nature (Lond) **198**, 382 (1963).
[57] J. Evers and G. Oehlinger, J. Solid State Chem. **62**, 133 (1986).
[58] Y. Takéuchi, Mineral. J. **2**, 90 (1957).
[59] A. Löhken, G. J. Reiß, D. Johrendt, and A. Mewis, Z. Anorg. Allg. Chem. **631**, 1144 (2015).
[60] J. Evers, G. Oehlinger, K. Polborn, and B. Sendlinger, J. Solid State Chem. **91**, 250 (1991).
[61] P. Bayliss, Am. Mineral. **74**, 1168 (1989).
[62] C. Lux, A. Mewis, S. Junk, A. Gruetz, and G. Michels, J. Alloys Compd. **200**, 135 (1993).
[63] R. Huch and W. Klemm, Z. Anorg. Allg. Chem. **329**, 123 (1964).
[64] R. Ferro, M. R. M. Raso, G. Rambaldi, and G. B. Bonino, Matematiche e Naturali. Rendiconti **36**, 498 (1964).
[65] See Supplemental Material at http://link.aps.org/supplemental/10.1103/PhysRevMaterials.6.084201 for the phonon dispersion of other 13 material samples with space group $P2_13$ (No. 198) and enlarged C-2 DP and S-1 WP, the magnetic ground state for 14 materials, and the phonon displacement details in the 9.0- to 10.6-THz frequency region.
[66] Z. M. Yu, Z. Y. Zhang, G. B. Liu, W. K. Wu, X. P. Li, R. W. Zhang, S. Y. A. Yang, and Y. G. Yao, Sci. Bull. **67**, 375 (2022).
[67] X. L. Feng, W. K. Wu, Z. M. Yu, and S. Y. A. Yang, Phys. Rev. B **104**, 115116 (2021).